

# Demonstration of Dispersion-Cancelled Quantum-Optical Coherence Tomography

Magued B. Nasr, Bahaa E. A. Saleh, Alexander V. Sergienko, and Malvin C. Teich\*

*Quantum Imaging Laboratory<sup>†</sup>, Departments of  
Electrical & Computer Engineering and Physics,  
Boston University, Boston, MA 02215*

## Abstract

We present an experimental demonstration of quantum optical coherence tomography (QOCT). The technique makes use of an entangled twin-photon light source to carry out axial optical sectioning. QOCT is compared to conventional optical coherence tomography (OCT). The immunity of QOCT to dispersion, as well as a factor of two enhancement in resolution, are experimentally demonstrated.

PACS numbers: 42.50.Nn, 42.50.Dv, 42.30.Wb

---

\* Email address: teich@bu.edu

† URL: <http://www.bu.edu/qil>

Optical coherence tomography (OCT) has become a versatile and useful biological imaging technique [1, 2, 3], particularly in ophthalmology [4], cardiology [5], and dermatology [6]. It is an interferometric scheme that makes use of a light source of short coherence time (broad spectrum) [7] to carry out axial sectioning of a biological specimen. Axial resolution is enhanced by increasing the spectral bandwidth of the source (sub-micrometer resolution has recently been achieved by using a light source with a bandwidth of 325 nm [8]). However, as the bandwidth is increased the effects of group-velocity dispersion becomes increasingly deleterious [9]. Various techniques have been used in attempts to counteract the effects of dispersion, but these require *a priori* knowledge of the dispersion intrinsic to the specimen [10].

A quantum version of OCT that makes use of an entangled twin-photon light source has recently been proposed [11]. A particular merit of quantum-optical coherence tomography (QOCT) is that it is inherently immune to dispersion by virtue of the frequency entanglement associated with the twin-photon pairs [12, 13, 14]. Moreover, for sources of the same bandwidth, the entangled nature of the twin photons provides a factor of two enhancement in resolution relative to OCT.

In this letter we report the first experimental demonstration of QOCT, and show that the technique is indeed insensitive to group-velocity dispersion. A parallel experiment using conventional OCT with a source of the same bandwidth is conducted to provide a direct comparison of the two techniques. Using the reflections from the two surfaces of a fused-silica sample buried under a 10-mm-thick ZnSe window (a highly dispersive material) as a sample, we obtain an improvement in resolution by a factor of approximately 5. This improvement arises from the concatenation of two effects: dispersion cancellation and the factor-of-two advantage.

We begin with a brief discussion of the principle underlying QOCT (for a comparative review of the theories of QOCT and OCT the reader is referred to Ref. [11]). A schematic of the QOCT arrangement is illustrated in Fig. 1. The entangled twin photons may be conveniently generated via spontaneous parametric down-conversion (SPDC) [15]. In this process a monochromatic laser beam of angular frequency  $\omega_p$ , serving as the pump, is sent to a second-order nonlinear optical crystal (NLC). A fraction of the pump photons disintegrate into pairs of downconverted photons. Both downconverted photons have the same polarization and central angular frequency  $\omega_0 = \omega_p/2$ , corresponding to type-I degenerate

SPDC. We direct our attention to a noncollinear configuration, in which the photons of the pairs are emitted in selected different directions (modes), denoted 1 and 2. Although each of the emitted photons has a broad spectrum in its own right, the sum of the angular frequencies must always equal  $\omega_p$  by virtue of energy conservation.

The twin-photon source is characterized by the frequency-entangled state

$$|\psi\rangle = \int d\Omega \zeta(\Omega) |\omega_0 + \Omega\rangle_1 |\omega_0 - \Omega\rangle_2, \quad (1)$$

where  $\Omega$  is the angular frequency deviation about the central angular frequency  $\omega_0$  of the twin-photon wave packet,  $\zeta(\Omega)$  is the spectral probability amplitude, and the spectral distribution  $S(\Omega) = |\zeta(\Omega)|^2$  is normalized such that  $\int d\Omega S(\Omega) = 1$ . For simplicity we assume  $S(\Omega)$  to be a symmetric function. Each photon of the pair resides in a single spatial mode, indicated by the subscripts 1 and 2 in Eq. (1).

The schematic illustrated in Fig. 1 has, at its heart, the two-photon interferometer considered by Hong, Ou, and Mandel (HOM) [16]. The conventional HOM configuration is modified by placing the sample to be probed in one arm and an adjustable temporal delay ( $\tau_q$ ) in the other arm. The entangled photons are directed to the two input ports of a symmetric beam splitter (BS). Beams 3 and 4 at its output ports are directed to two single-photon-counting detectors,  $D_1$  and  $D_2$ , respectively. The coincidence rate of photons arriving at the two detectors,  $C(\tau_q)$ , is recorded within a time window determined by a coincidence circuit (indicated by  $\otimes$ ).

An experiment is conducted by sweeping the temporal delay  $\tau_q$  and recording the interferogram  $C(\tau_q)$ . If a mirror were to replace the sample, this would trace out a dip in the coincidence rate whose minimum would occur when arms 1 and 2 of the interferometer had equal path lengths. This dip would result from interference of the two photon-pair probability amplitudes, *viz.* reflection or transmission of both photons at the beam splitter.

For simplicity, we neglect losses in this exposition. A weakly reflecting sample is then described by a transfer function  $H(\omega)$ , characterizing the overall reflection from all structures that comprise the sample, at angular frequency  $\omega$ :

$$H(\omega) = \int_0^\infty dz r(z, \omega) e^{i2\phi(z, \omega)}. \quad (2)$$

The quantity  $r(z, \omega)$  is the complex reflection coefficient from depth  $z$  and  $2\phi(z, \omega)$  is the round-trip phase accumulated by the wave while travelling through the sample to depth  $z$ .

As shown previously [11], the coincidence rate  $C(\tau_q)$  is then given by

$$C(\tau_q) \propto \Lambda_0 - \text{Re} \{ \Lambda(2\tau_q) \}, \quad (3)$$

where

$$\Lambda_0 = \int d\Omega |H(\omega_0 + \Omega)|^2 S(\Omega) \quad (4)$$

and

$$\Lambda(\tau_q) = \int d\Omega H(\omega_0 + \Omega) H^*(\omega_0 - \Omega) S(\Omega) e^{-i\Omega\tau_q} \quad (5)$$

represent the constant and varying contributions, respectively. The interferogram  $C(\tau_q)$  yields useful information about the transfer function  $H(\omega)$  and hence about the reflectance  $r(z, \omega)$  [11].

The details of the QOCT experimental arrangement are shown in Fig. 2. For QOCT scans, the dotted components (mirrors  $M_1$  and  $M_2$ , as well as detector  $D_3$ ) are removed. The entangled photons, centered about  $\lambda_0 = 812$  nm and emitted in a non-collinear configuration, travel in beams 1 and 2. The photon in beam 1 travels through a temporal delay  $\tau_q$  before it enters the input port of the first beam splitter,  $BS_1$ . The second photon in beam 2 goes through a second beam splitter,  $BS_2$ , which ensures normal incidence onto the sample. The photon returned from the sample is directed to the other input port of  $BS_1$ . Beams 3 and 4, at the output of  $BS_1$ , are directed to  $D_1$  and  $D_2$ , respectively.

For OCT scans, the photons in beam 1 are discarded and mirrors  $M_1$  and  $M_2$  remain in place (see Fig. 2). The photons in beam 2 serve as a short-coherence-time light source. The reflections from the sample and mirror  $M_1$ , after recombination at beam splitter  $BS_2$  are directed to detector  $D_3$  via mirror  $M_2$ . The result is a simple Michelson interferometer, the standard configuration for OCT. To conduct an experiment, the temporal delay  $\tau_c$  is swept and the singles rate is recorded, forming the OCT interferogram  $I(\tau_c)$ . This arrangement permits a fair comparison between QOCT and OCT since both make use of a light source with identical spectrum.

The initial experiment makes use of a thin fused-silica window as the sample. The transfer function  $H(\omega)$  is then given by

$$H(\omega) = r_1 + r_2 e^{i2\omega nL/c}, \quad (6)$$

where the reflectances from the front and back surfaces are  $|r_1|^2 = |r_2|^2 = 0.04$  at normal incidence;  $L = 90$   $\mu\text{m}$  is the sample thickness (which is greater than the 37- $\mu\text{m}$  coherence

length of the source),  $c$  is the speed of light in vacuum, and  $n \approx 1.5$  is the refractive index of the fused silica (which is taken to be independent of  $\omega$  by virtue of the low dispersiveness of the material). Under these conditions, Eqs. (4), (5), and (6) yield

$$\Lambda_0 = |r_1|^2 + |r_2|^2 \quad (7)$$

and

$$\Lambda(\tau_q) = |r_1|^2 s(\tau_q) + |r_2|^2 s(\tau_q - 2\tau_d) + 2 \operatorname{Re} \{r_1 r_2^* s(\tau_q - \tau_d) e^{i\omega_p n L/c}\}, \quad (8)$$

where  $s(\tau_q)$  is the Fourier transform of the source spectrum  $S(\Omega)$ . Substituting Eqs. (7) and (8) into Eq. (3) yields an interferogram that contains the three varying terms in Eq. (8).

The first two terms in Eq. (8) are dips arising from reflections from each of the two surfaces. They are separated by  $\tau_d = 2nL/c$  and are expected to exhibit 50% visibility since  $|r_1|^2 = |r_2|^2$ . The third term, which appears midway between the two dips, arises from interference between the probability amplitudes associated with these reflections. This term changes from a hump to a dip depending on the values of  $\omega_p$ ,  $n$ ,  $L$ , and the arguments of  $r_1$  and  $r_2$ .

The experimental QOCT interferogram for this sample, normalized to  $\Lambda_0$ , is plotted in Fig. 3a. The two dips, separated by the optical path length of the sample  $nL = 135 \mu\text{m}$ , exhibit 45% visibility, in close agreement with the theoretically expected value of 50%. The abscissa is represented in units of the scaled temporal delay  $c\tau/2$ , representing the physical displacement of the delay line, so that  $\tau$  stands for  $\tau_q$  and  $\tau_c$  alike.

The OCT interferogram for the same sample is expected to consist of two interference-fringe envelopes, each with visibility calculated to be 30%, separated by  $\tau_d$ . The experimental OCT interferogram for this sample, normalized to the constant background, is shown in Fig. 3b. The centers of the envelopes, separated by  $nL = 135 \mu\text{m}$ , exhibit 28% visibility.

It is apparent that the 18.5- $\mu\text{m}$  FWHM of the dips observed in QOCT provides a factor of 2 improvement in resolution over the 37- $\mu\text{m}$  FWHM of the envelopes observed in OCT. This improvement, which is in accord with theory [11], ultimately results from the entanglement inherent in the nonclassical light source used in QOCT.

To demonstrate the dispersion-cancellation capability of QOCT, we bury the sample under a highly dispersive medium and carry out a QOCT/OCT experiment, as described above. The transfer function of this composite sample is then  $H_{\text{disp}}(\omega) = H(\omega) e^{i2\beta(\omega)d}$ , where the transfer function of the fused-silica window  $H(\omega)$  is given by Eq. (6),  $\beta(\omega)$  is the

wave number in the dispersive medium, and  $d$  is the thickness of the dispersive medium. We expand  $\beta(\omega_0 + \Omega)$  to second order in  $\Omega$ :  $\beta(\omega_0 + \Omega) \approx \beta_0 + \beta'\Omega + \beta''\Omega^2$ , where  $\beta'$  is the inverse of the group velocity  $v_0$  at  $\omega_0$ , and  $\beta''$  represents group-velocity dispersion (GVD) [7].

Substituting  $H_{\text{disp}}(\omega)$  into Eq. (5), the QOCT varying term for the buried sample turns out to be

$$\Lambda_{\text{disp}}(\tau_q) = \Lambda(\tau_q - 2\beta'd), \quad (9)$$

which is simply a displaced version of the result obtained for the sample in air, as provided in Eq. (8). Neither  $\beta_0$  nor the GVD parameter  $\beta''$  appear in Eq. (9); nor, in fact, do any higher even-order terms. The cancellation of GVD is an important signature of QOCT. In OCT  $\beta''$  does not cancel and the result is a degradation of depth resolution and a reduction of the signal-to-noise ratio [10].

In the experimental realization, the fused-silica window is buried beneath two cascaded 5-mm-thick windows of highly dispersive ZnSe, slightly canted with respect to the incident beam to divert back-reflections, as shown at the top of Fig. 4. The GVD coefficient for ZnSe is  $\beta'' = 5 \times 10^{-25} \text{ s}^2\text{m}^{-1}$  at  $\lambda_0 = 812 \text{ nm}$ , which is 25 times greater than that for fused silica.

Figure 4a shows the normalized QOCT interferogram for the buried sample. As predicted in Eq. (9), the widths of the dips remain  $18.5 \mu\text{m}$ , just as they were in the absence of the dispersive medium (see Fig. 3a). *Thus the resolution of the QOCT scan is unaffected by the presence of the dispersive medium.* The hump between the two dips in the QOCT interferogram in Fig. 4a is also unaffected by the presence of the dispersive medium. This would not be the case, however, if the dispersive material were between the reflecting surfaces rather than outside of them [11]. On the other hand, the interference-fringe envelopes in the normalized OCT interferogram displayed in Fig. 4b are *broadened* from  $37$  to  $92 \mu\text{m}$  as a result of dispersion.

It is also of interest to compare the visibility of the interferograms. Diverted reflection losses are not expected to reduce the visibility of the QOCT features, whereas this benefit does not accrue to OCT [11]. The robustness of QOCT in this connection is evident in Fig. 4a, where the reduction of visibility (in comparison with Fig. 3a) arises only from misalignment. In Fig. 4b, on the other hand, the OCT interferogram suffers a substantially greater loss of visibility (in comparison with Fig. 3b), as a result of both dispersion and

diverted losses from the four uncoated ZnSe surfaces.

In conclusion, we have carried out proof-of-principle experiments demonstrating the successful operation of a new axial optical sectioning technique, quantum optical coherence tomography (QOCT). We have experimentally demonstrated the two principal advantages that stem from the frequency entanglement of the twin-photon source: dispersion cancellation and resolution doubling.

This work was supported by the National Science Foundation; by the Center for Subsurface Sensing and Imaging Systems (CenSSIS), an NSF Engineering Research Center; and by the David & Lucile Packard Foundation. We are grateful to G. Di Giuseppe, A. Abouraddy, and M. Hendrych for assistance with the experiments and helpful comments.

- 
- [1] D. Huang, E. A. Swanson, C. P. Lin, J. S. Schuman, W. G. Stinson, W. Chang, M. R. Hee, T. Flotte, K. Gregory, C. A. Puliafito, and J. G. Fujimoto, *Science* **254**, 1178 (1991).
  - [2] J. G. Fujimoto, M. E. Brezinski, G. J. Tearney, S. A. Boppart, B. Bouma, M. R. Hee, J. F. Southern, and E. A. Swanson, *Nature Med.* **1**, 970 (1995).
  - [3] J. M. Schmitt, *IEEE J. Sel. Topics Quantum Electron.* **5**, 1205 (1999).
  - [4] M. R. Hee, J. A. Izatt, E. A. Swanson, D. Huang, J. S. Schuman, C. P. Lin, C. A. Puliafito, and J. G. Fujimoto, *Arch. Ophthalmol. (Chicago)* **113**, 325 (1995).
  - [5] M. E. Brezinski, G. J. Tearney, N. J. Weissman, S. A. Boppart, B. E. Bouma, M. R. Hee, A. E. Weyman, E. A. Swanson, J. F. Southern, and J. G. Fujimoto, *Heart* **77**, 397 (1997).
  - [6] J. Welzel, *Skin Res. Technol.* **7**, 1 (2001).
  - [7] B. E. A. Saleh and M. C. Teich, *Fundamentals of Photonics* (Wiley, New York, 1991).
  - [8] B. Povazay, K. Bizheva, A. Unterhuber, B. Hermann, H. Sattmann, A. F. Fercher, W. Drexler, A. Apolonski, W. J. Wadsworth, J. C. Knight, P. St. J. Russell, M. Vetterlein, and E. Scherzer, *Opt. Lett.* **27**, 1800 (2002).
  - [9] C. K. Hitzenberger, A. Baumgartner, W. Drexler, and A. F. Fercher, *J. Biomed. Opt.* **4**, 144 (1999).
  - [10] A. F. Fercher, C. K. Hitzenberger, M. Sticker, R. Zawadzki, B. Karamata, and T. Lasser, *Opt. Comm.* **204**, 67 (2002).
  - [11] A. F. Abouraddy, M. B. Nasr, B. E. A. Saleh, A. V. Sergienko, and M. C. Teich, *Phys. Rev.*

- A **65**, 053817 (2002).
- [12] J. D. Franson, Phys. Rev. A **45**, 3126 (1992).
- [13] A. M. Steinberg, P. G. Kwiat, and R. Y. Chiao, Phys. Rev. A **45**, 6659 (1992); Phys. Rev. Lett. **68**, 2421 (1992).
- [14] T. S. Larchuk, M. C. Teich, and B. E. A. Saleh, Phys. Rev. A **52**, 4145 (1995).
- [15] L. Mandel and E. Wolf, *Optical Coherence and Quantum Optics* (Cambridge, New York, 1995), ch. 22.
- [16] C. K. Hong, Z. Y. Ou, and L. Mandel, Phys. Rev. Lett. **59**, 2044 (1987).

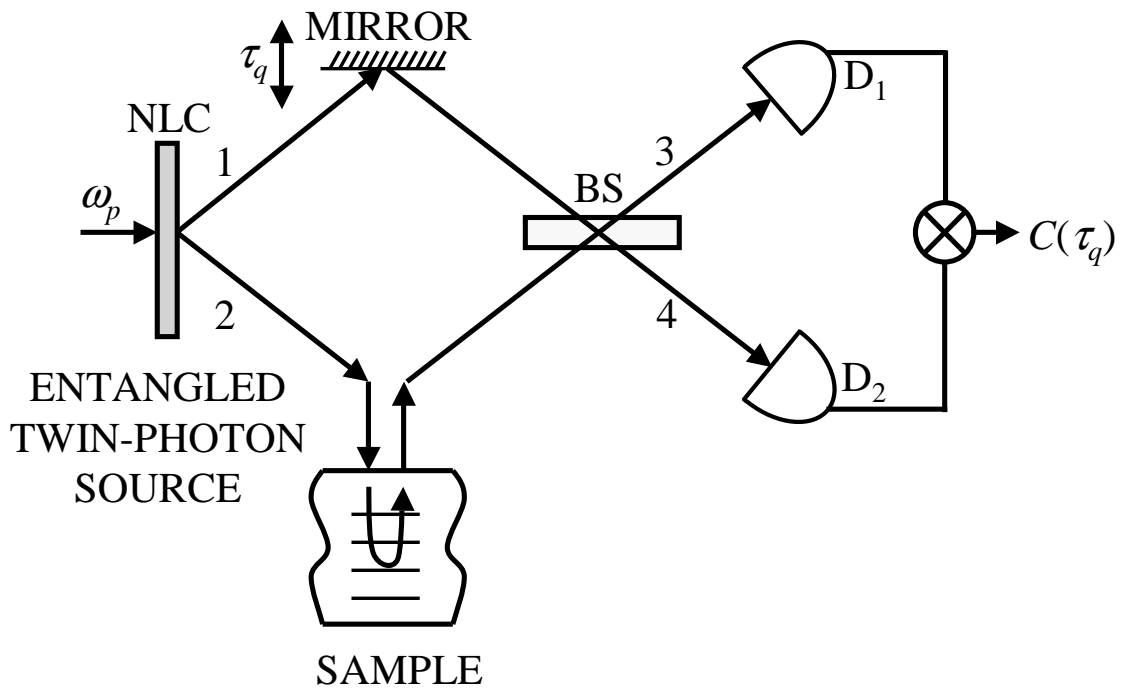


FIG. 1: Schematic of quantum-optical coherence tomography (QOCT). A monochromatic laser of angular frequency  $\omega_p$  pumps a nonlinear crystal (NLC), generating pairs of entangled photons. BS stands for beam splitter and  $\tau_q$  is an adjustable temporal delay.  $D_1$  and  $D_2$  are single-photon-counting detectors that feed a coincidence circuit indicated by the symbol  $\otimes$ . The outcome of an experiment is the coincidence rate  $C(\tau_q)$ .

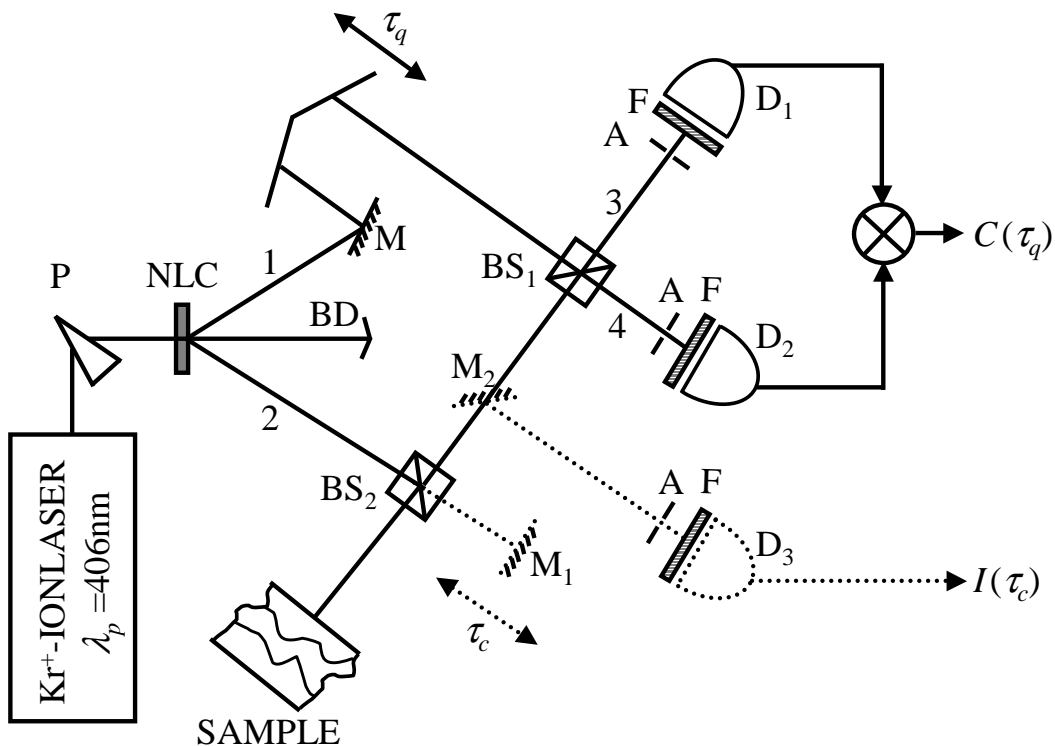


FIG. 2: Experimental arrangement for quantum/classical optical coherence tomography QOCT/OCT. A monochromatic  $\text{Kr}^+$ -ion laser operated at  $\lambda_p = 406$  nm pumps an 8-mm-thick type-I  $\text{LiIO}_3$  nonlinear crystal (NLC) after passage through a prism, P, and an aperture (not shown), which remove the spontaneous glow of the laser tube. BD stands for beam dump (to block the pump), BS for beam splitter, M for mirror, A for 2.2-mm aperture, F for long-pass filter with cutoff at 725 nm, and D for single-photon-counting detector (EG&G, SPCM-AQR-15). The quantities  $\tau_q$  and  $\tau_c$  represent temporal delays. For QOCT scans, the dotted components  $M_1$ ,  $M_2$  and  $D_3$  are removed,  $\tau_q$  is swept, and the coincidence rate  $C(\tau_q)$  is measured within a 3.5-nsec time window. For OCT scans, beam 1 is discarded (beam 2 serves as the short-coherence-time light source),  $\tau_c$  is swept, and the singles rate  $I(\tau_c)$  is recorded.

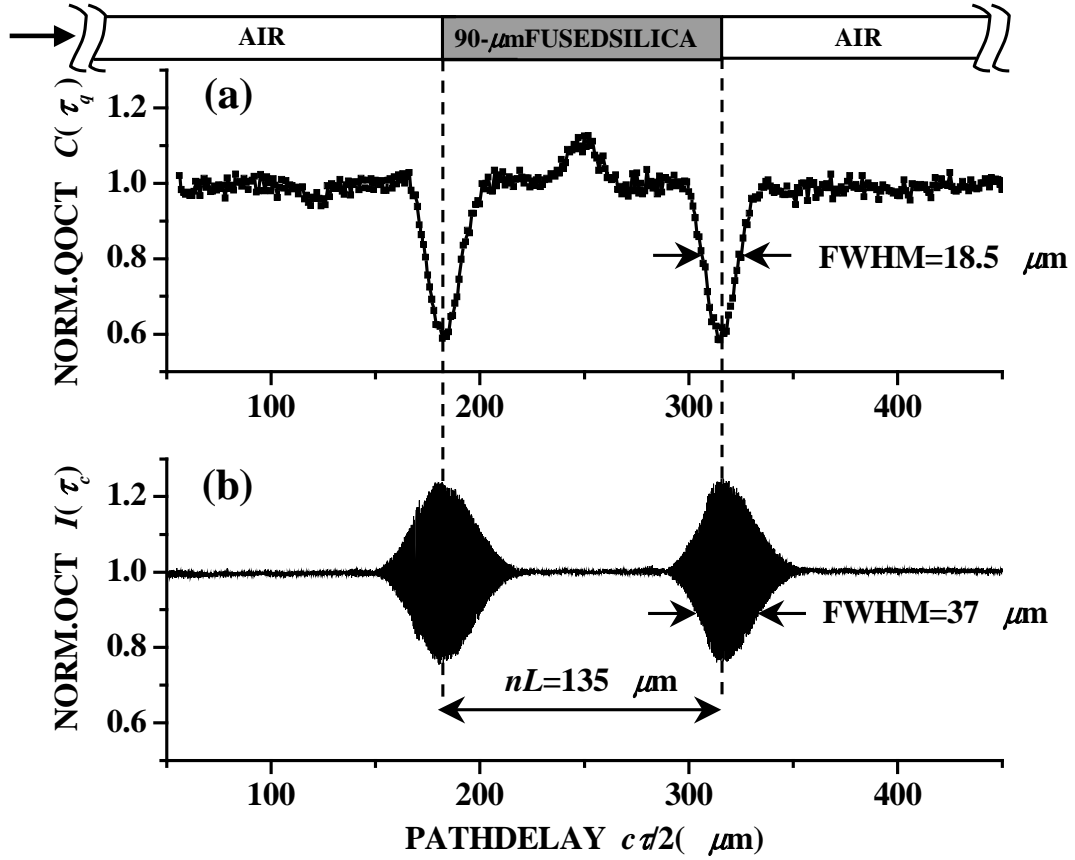


FIG. 3: QOCT and OCT normalized interferograms for a 90- $\mu\text{m}$  fused-silica window in air (as shown at top of figure). The abscissa is the scaled temporal delay  $c\tau/2$ , which represents displacement of the delay line ( $\tau$  therefore represents both  $\tau_q$  and  $\tau_c$ ). (a) Coincidence rate  $C(\tau_q)$  normalized to  $\Lambda_0$  (the QOCT normalized interferogram). (b) Singles rate  $I(\tau_c)$  normalized to constant background (the normalized OCT interferogram).

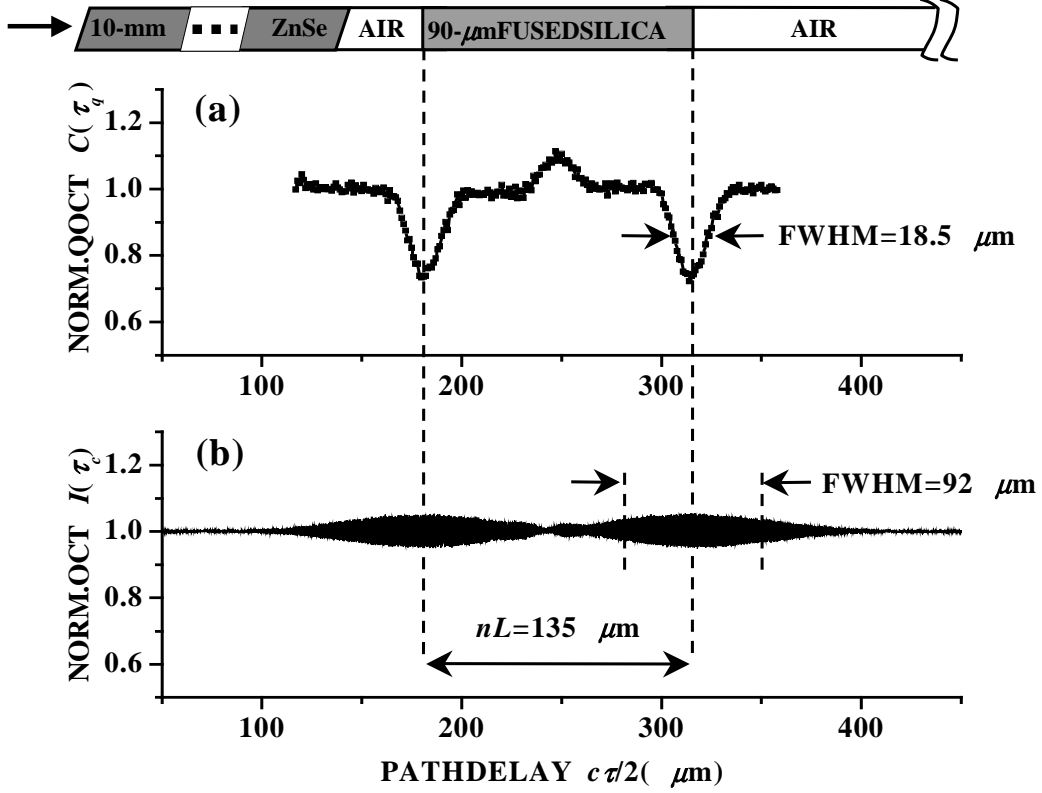


FIG. 4: QOCT and OCT normalized interferograms for a 90- $\mu\text{m}$  fused-silica window buried beneath two cascaded 5-mm-thick windows of highly dispersive ZnSe. As shown at the top of the figure, the ZnSe is slightly canted with respect to the incident beam (arrow) to divert back-reflections. The abscissa is the scaled temporal delay  $c\tau/2$ , which represents displacement of the delay line ( $\tau$  therefore represents both  $\tau_q$  and  $\tau_c$ ). (a) Coincidence rate  $C(\tau_q)$  normalized to  $\Lambda_0$  (the QOCT normalized interferogram). (b) Singles rate  $I(\tau_c)$  normalized to constant background (the normalized OCT interferogram).